Spectral Fresnel filter for pulsed broadband terahertz radiation

Cite as: AIP Advances **10**, 125104 (2020); https://doi.org/10.1063/5.0024456
Submitted: 07 August 2020 . Accepted: 05 November 2020 . Published Online: 01 December 2020

Xinrui Liu, Maksim S. Kulya, Nikolay V. Petrov, Yaroslav V. Grachev, Mingzhao Song, Anton N. Tcypkin, Sergey A. Kozlov, and Xi-Cheng Zhang

Spectral Fresnel filter for pulsed broadband terahertz radiation

Cite as: AIP Advances 10, 125104 (2020); doi: 10.1063/5.0024456
Submitted: 7 August 2020 • Accepted: 5 November 2020 •
Published Online: 1 December 2020

Xinrui Liu,[1] **Maksim S. Kulya,**[1,2] **Nikolay V. Petrov,**[1] **Yaroslav V. Grachev,**[1,3] **Mingzhao Song,**[4,a)] **Anton N. Tcypkin,**[1] **Sergey A. Kozlov,**[1] **and Xi-Cheng Zhang**[1,5]

AFFILIATIONS

[1] Department of Photonics and Optoinformatics, ITMO University, St. Petersburg 197101, Russia
[2] Faculty of Information Technology and Communication Sciences, Tampere University, Tampere FI-33014, Finland
[3] Photovoltaics Laboratory, Ioffe Institute, St. Petersburg 194021, Russia
[4] Department of Physics and Engineering, ITMO University, St. Petersburg 197101, Russia
[5] The Institute of Optics, University of Rochester, Rochester, New York 14627, USA

[a)] **Author to whom correspondence should be addressed:** kevinsmz@foxmail.com

ABSTRACT

We proposed a simple and cost-effective method to manipulate the temporal and spectral properties of pulsed terahertz waves. A deep modulation of a pulse spectrum was both numerically and experimentally verified using Fresnel apertures with a radius ranging from several to several tens of the central wavelength of the broadband terahertz radiation. N-fold frequency minima were formed in the spectrum at a specific axial position behind the filter. Non-paraxial properties of this filter were also analyzed. A significant value (35%) of the ratio of the longitudinal to the transverse field component at the filter frequency was obtained. The measured results agree well with the simulation and theoretical predictions. The property of such a diffractive Fresnel notch filter can benefit the generation of longitudinal terahertz fields and relevant applications.

I. INTRODUCTION

Control over parameters of pulsed broadband radiation with an ultra-short duration is an important task for many applications. A variety of methods and devices have been proposed to control the spectral composition of ultra-broadband terahertz (THz) pulses, consisting essentially of a single oscillation of the electromagnetic field,[1] for instance, plasmonic metamaterials,[2] parallel-plate waveguides,[3] and pulse shapers,[4] to name a few. To effectively modulate THz waves, diffraction devices can be used as good tools due to their simpler fabrication process in the THz range than other frequency ranges.[5] As a diffractive device, Fresnel zone plate (FZP) lenses and lens antennas have been frequently used as radiation, modulation, and imaging devices in THz electronic systems.[6–9] However, a simple circular aperture has not been discussed as a device or as a part of a device before. The diffraction phenomenon on a circular aperture has been well discussed in the paraxial region (the aperture radius much larger than the wavelength, $R \gg \lambda$),[10] and the propagation properties of the highly non-paraxial region ($R < \lambda$) has also been introduced for non-paraxial beams.[11] However, the intermediate region (the aperture radius is of several wavelengths) has not been fully investigated so far.

Contrary to previous studies, in this letter, we introduced a simple and low-cost Fresnel filter (FF) that suppresses a certain set of spectral components of broadband THz radiation resulting from destructive interference of even number of Fresnel zones for the determined axial position. In general, the proposed filter can be applied not only in the THz frequency range but also in any range of the electromagnetic spectrum. Particular attention in the design of the FF in this work is paid to the analysis of spatial and spectral visibility depending on the ratio of the size of the Gaussian beam to the size of the aperture. Vectorial characteristics, in particular, longitudinal electromagnetic field components, were mostly evinced and studied at the focal waist (see, e.g., Ref. 12), and evanescent waves were analyzed for the broadband THz spectrum after the FF.[13]

II. RESULTS

Modern pulsed THz sources can generate linearly polarized waves consisting of one complete field oscillation which can be modeled in the temporal domain as[14]

$$E(x,y,t) = E_0 \frac{t}{\tau} e^{-\frac{t^2}{\tau^2}} e^{-\frac{x^2+y^2}{\rho^2}}, \tag{1}$$

where E is the electric field, x and y are the Cartesian coordinates transverse to the beam propagation direction z, E_0 characterizes the amplitude of the electric field, t is the time, τ is the pulse duration, and ρ is the transverse size of the Gaussian beam. Equation (1) is an approximation of the THz pulse generated through the optical rectification of femtosecond pulses in crystals,[15] or by a photoconductive semiconductor emitter,[16] or air plasma[17] irradiated by pulsed femtosecond lasers. The spectral representation of $E(x,y,t)$ can be obtained by Fourier integral in the time domain with the analytical solution

$$G(x,y,\nu) = \int_{-\infty}^{\infty} E(x,y,t) e^{-i2\pi\nu t} dt$$
$$= G_0 \frac{\nu}{\nu_0} e^{-\frac{1}{2}\left(\frac{\nu}{\nu_0}\right)^2} e^{-\frac{x^2+y^2}{\rho^2}}, \tag{2}$$

where $\nu_0 = \frac{1}{\pi\tau}$ and $G_0 = \frac{-iE_0}{\sqrt{\pi}\nu_0}$. It characterizes the spectral amplitude of the pulse in Eq. (1), and ν_0 is the frequency corresponding to the maximum of spectral density. The maximum values of spectral density and electric field strength are $G_{\max}(\nu_0) = \frac{\sqrt{\pi}\tau E_0}{e}$ and $E_{\max} = \frac{1}{\sqrt{2e}}E_0$, respectively, while $t = \pm\frac{\tau}{\sqrt{2}}$.

The FF operation principle is shown in Fig. 1. A Gaussian THz beam used as an initial input signal described by Eq. (1) is shown in Fig. 1(a). An opaque mask with a circular aperture of radius R located at the position $z = 0$ is used as a filter to modulate the THz spatial spectrum. At the observation plane $z = z_p$, which corresponds to the even number N of Fresnel zones ($N = 2, 4, 6, \ldots$) for frequencies ν_f, a strong diffraction phenomenon leads to the formation of spectral minima localized at the optical axis.

The FF properties are defined by the observation distance and the radius of the aperture. In particular, it means that for a collimated wavefront, we can estimate the distance z_p, at which the aperture can be considered as N Fresnel zones for the spectral component of broadband THz radiation with the frequency ν_f,

$$z_p(N,\lambda_f) = \left(R^2 - \frac{N^2}{4}\lambda_f^2\right)/N\lambda_f, \quad \lambda_f = c/\nu_f. \tag{3}$$

Here, c is the speed of light in vacuum. Thus, by changing the observation distance, we may adjust the spectral component to be filtered. Alternatively, rewriting the equation for the radius R as

$$R(N,\lambda_f) = N\lambda_f\left(z_p + \frac{N}{4}\lambda_f\right) \tag{4}$$

gives us tuning of the filtered spectral component by a simple change of the aperture radius for a fixed z_p. Figure 2(a) explains the ability of the described FF to vary the filtered frequency ν_f depending on the mentioned parameters: observation distance z_p and aperture radius R.

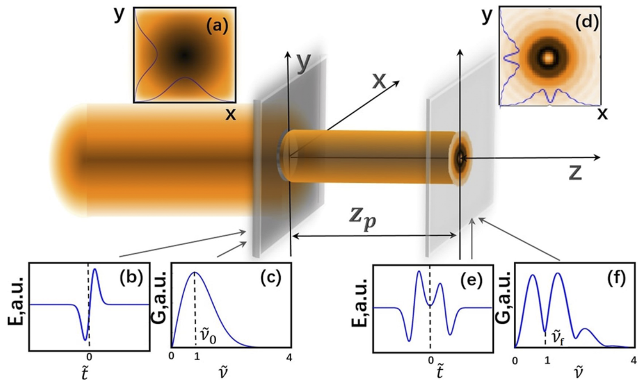

FIG. 1. Scheme of the pulsed THz wavefront propagation through the FF. Insets are the transverse structure of the field with the cross sections marked by blue lines [(a) and (d)], the corresponding temporal form [(b) and (e)], and the modulus of its spectrum [(c) and (f)] for the initial beam and field at distance z_p with diffraction minima.

In this work, we considered a general Gaussian profile beam with a beam width ρ and its particular case, namely, an infinite uniform plane wave (ρ tends to infinity). The ratio of the Gaussian beam width ρ to the aperture radius is one of the key parameters of the FF. To demonstrate the tunability of the proposed filter, we first plot the filter frequency ν as a function of the aperture radius R and the

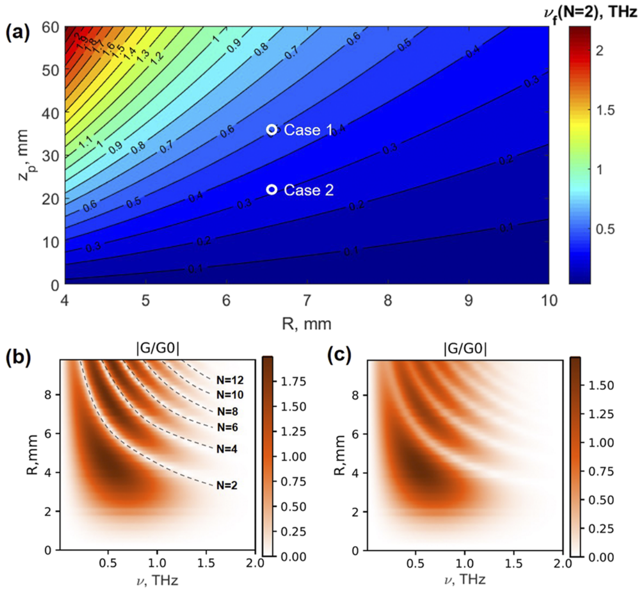

FIG. 2. Demonstration of the tunability of the proposed FF: (a) the dependence of operation frequency ν_f for $N = 2$ as a function of the aperture radius R and observation distance z_p, where both further considered cases are verified and marked by white dots and the normalized modulus of the temporal spectrum at $z_p = 34$ mm for (b) a Gaussian beam with an infinite beam width ($\rho = \infty$) and (c) for $\rho = 8$ mm.

observation distance z_p based on Eq. (3) in Fig. 2(a). Figures 2(b) and 2(c) illustrate the normalized modulus of the temporal spectrum that contains explicit minima only for a sufficiently large ρ/R [Fig. 2(b)], which means the size of the Gaussian beam is much larger than the size of the aperture, and therefore, the beam center passing through the aperture can be considered as a quasi–uniform plane wave. In the case of a limited beam width [Fig. 2(c), $\rho = 8$ mm], low frequencies will undergo weaker diffraction, which leads to incomplete filtering of these spectral components.

Usually, the central wavelength λ_0 is pre-defined by the source. Therefore, λ_0 and τ can be used to normalize almost all parameters to generalize the results for more cases independent of the wavelength: $\widetilde{t} = \frac{t}{\tau}$, $\widetilde{\nu} = \frac{\nu}{\nu_0}$, $\widetilde{x} = \frac{x}{\lambda_0}$, $\widetilde{y} = \frac{y}{\lambda_0}$, and $\widetilde{z} = \frac{z}{\lambda_0}$, where $\lambda_0 = c/\nu_0$, and only two parameters, namely, $\widetilde{\rho} = \frac{\rho}{\lambda_f}$ and $\widetilde{R} = \frac{R}{\lambda_f}$ are normalized on the filtered wavelength as an important one for the filter design.

Further results are obtained for the parameters and summarized in Table I. We consider two filter designs: when the filtered frequency $\nu_f(N = 2)$ coincides with ν_0 [Fig. 1(f) and case 1 in Table I, all in a simulation] and when this condition is not satisfied (case 2 in Table I, for an experiment and related simulation). Note that in the general case, one can observe the additional minima when multiple frequencies ν_f exist in the broadband spectrum [see, e.g., Figs. 1(f), 2(b), and 2(c)]. Thus, our FF designs correspond to both cases when an aperture radius corresponds to units and tens of filtered wavelengths λ_f and wavelength of the maximum spectral density λ_0. In the first case, $\widetilde{R} \approx 11$ reveals the non-paraxial properties of broadband THz radiation characterized by the presence of not only a transverse but also the longitudinal component of the field.

Experimental measurements and data processing have been conducted by THz pulse time-domain holography (PTDH). Theoretical studies, experimental setup, and validity of experimental and simulation results were described in other works.[18,19] In the main aspects, the principles of raster scan imaging based on THz time-domain spectroscopy are used in our experimental setup. The only main difference of the THz PTDH scheme against TDS is the measurement of the wavefront by a raster-scanning diaphragm instead of measurement in the focal plane, as explained in detail in Refs. 18 and 19. To analyze the propagation of the wavefront $G(x, y, \nu, z)$ to the arbitrary plane, we used the spectral approach described, applied, and probated in the works.[18–23] In particular, in Ref. 20, authors demonstrated its feasibility for paraxial and non-paraxial propagation of electromagnetic waves in the case of broadband single-cycle THz radiation.

Figure 3 shows the propagation dynamics of transverse and longitudinal components for an initially uniform plane wave passing through the circular aperture. The wave parameters in that experiment correspond to case 1, and are provided in Table I. The longitudinal field component was calculated from the transverse one in accordance with analytical equations (see Refs. 20 and 23). The results are presented both in spectral and temporal domains at distances $z = 1$ mm (immediately after the filter plane, left column in Fig. 3) and $\widetilde{z}_p = 56$ (right column in Fig. 3). The diffraction resulted in a broadening of the temporal structure as well as in an additional pulse oscillation. Comparing Figs. 3(a) and 3(e), one can find a significant diffraction pattern formed in the spectral domain. In the plane, corresponding to the second Fresnel zone for frequency $\nu_f(N = 2) = \nu_0$, a diffraction of the transverse component is implemented in the formation of the spectral minimum localized at the optical axis. The longitudinal component shows the non-paraxial character of the THz field behind the aperture [Figs. 3(b) and 3(f)]. Although its electric field is weaker than the transverse component, its structure can be still recognized from the simulation data.

It was calculated that the ratio of the evanescent wave amplitude to the transverse traveling wave amplitude for $\widetilde{R} = 10.7$ of the

TABLE I. Parameters used in the given work.

Case	τ (ps)	ν_0 (THz)	$\nu_f(N = 2)$ (THz)	$\widetilde{z}_p$	$\widetilde{\rho}$	$\widetilde{R}$
1	0.45	0.5	0.5	56	1–170	10.7
2	0.7	0.33	0.3	22	10.8	6.4

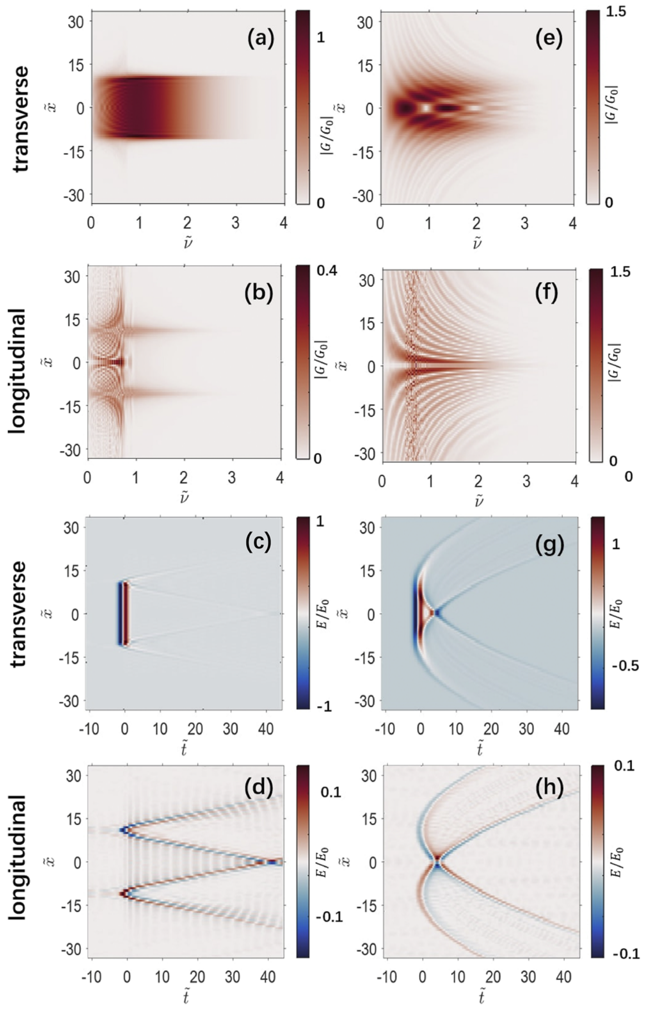

FIG. 3. Normalized transverse [(a), (c), (e), and (g)] and longitudinal [(b), (d), (f), and (h)] components of the temporal spectrum [(a) and (b)] and [(e) and (f)] and electric field amplitudes [(c) and (d)] and [(g) and (h)] at distances $z = 1$ mm (left column) and $\widetilde{z} = \widetilde{z}_p$ (right column).

Gaussian beam was about 7%, or equivalently 0.3% of the intensity. The amplitude of 7% was calculated as the sum of spectral density of evanescent waves divided by the sum of the spectral density of the traveling wave. In addition, 0.3% is a result of this ratio attributed to the squares of these spectral densities.

To estimate the relation between longitudinal and transverse components whose dynamics are shown in Fig. 3, we can calculate the integral of the wave intensity ratio with respect to time,

$$I_{E_z/E_x}(\tilde{x},\tilde{y}=\tilde{y}_0,\tilde{z}) = \frac{\int_{-\infty}^{\infty} E_z\left(\tilde{x},\tilde{y}=\tilde{y}_0,\tilde{t},\tilde{z}\right)^2 d\tilde{t}}{\int_{-\infty}^{\infty} E_x\left(\tilde{x},\tilde{y}=\tilde{y}_0,\tilde{t},\tilde{z}\right)^2 d\tilde{t}}. \qquad (5)$$

This relation significantly increases with spreading toward the beam periphery [see Fig. 4(a)]. However, when analyzing this relation I_{E_z/E_x} vs propagation distance, we pay the attention especially to the beam center [see Fig. 4(b)]. Quantitatively, it is useful to analyze the square root of this value. In the initial plane $\tilde{z} = 0$, the relation $\sqrt{(I_{E_z/E_x})}$ could achieve about 20% at the optical axis. It decreases further down to 5% at distance $\tilde{z} = \tilde{z}_p$. This behavior could be explained by analyzing Fig. 3. It can be observed in Figs. 3(g) and 3(h) that in the peripheral regions, the transverse field component is much smaller than the longitudinal component. On the other hand, the spectral density ratio of the longitudinal to the transverse components at a fixed frequency is also informative. Figures 4(d)–4(f) show how $|G_z/G_x|$ changes over distance for the frequency $\tilde{\nu}_f(N = 2) = 1$. It is worth noting that for some regions that are either far from the optical axis ($|\tilde{x}| > 8$) or in the vicinity after the aperture ($\tilde{z} < 17$), this ratio $|G_z/G_x|$ becomes larger than unity, whereas it decreases as the wave propagates to the rest of the areas.

How the spectral ratio evolves along the beam axis is also of great interest. Figure 4(f) shows the plot of the spectral ratio on the central cross-section, where it takes the highest value of 35% at distance $z = z_p$, revealing a significant non-paraxial effect. Such a high value is caused by a process of decreasing the transverse component due to its diffraction in the even Fresnel zone. The consequence of that process is the increasing of the ratio of the weak longitudinal component to the minimized transverse one.

Figure 5 illustrates the normalized (in the aperture plane) spatial distribution of the transverse spectral amplitude [(a) and (b)] in terms of $G(\tilde{x},\tilde{y},\tilde{\nu} = 1,\tilde{z} = \tilde{z}_p)$ (a) and the spatio-spectral distribution [(d) and (e)]. From Figs. 5(a) and 5(d), we observe the spectral minimum at frequency $\tilde{\nu}_f(N = 2) = 1$ in the beam center. Cross-sections marked by black lines 1 and 2 also illustrate this spectral gap [Figs. 5(b) and 5(e)]. Here, lines of different colors correspond to different ratios of $\tilde{\rho}/\tilde{R}$.

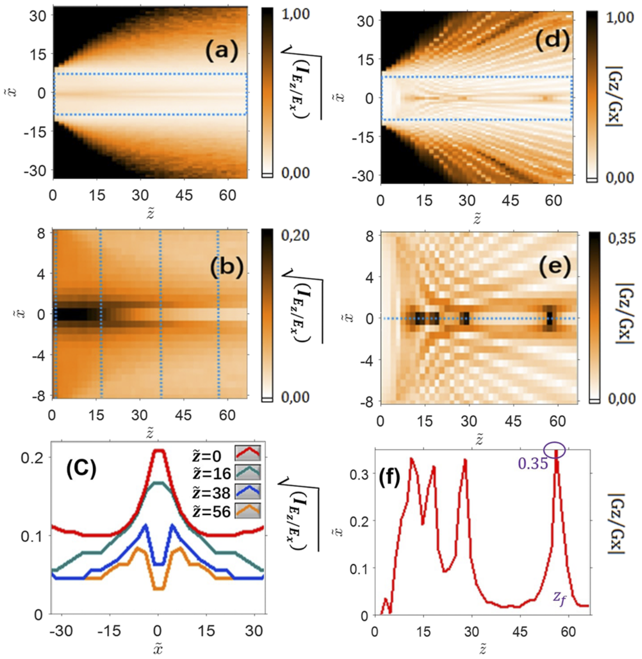

FIG. 4. Transverse and longitudinal components' ratios in the integral form $\sqrt{(I_{E_z/E_x})}$ (left column) and in the spectral amplitude form $|G_z/G_x|$ for filter frequency ν_f (right column): [(a) and (d)] are for the entire considered spatial domain; [(b) and (e)] are the scaling cases of (a) and (d); [(c) and (f)] are one-dimensional views of cross and axial sections along the dotted lines in [(b) and (e)] correspondingly.

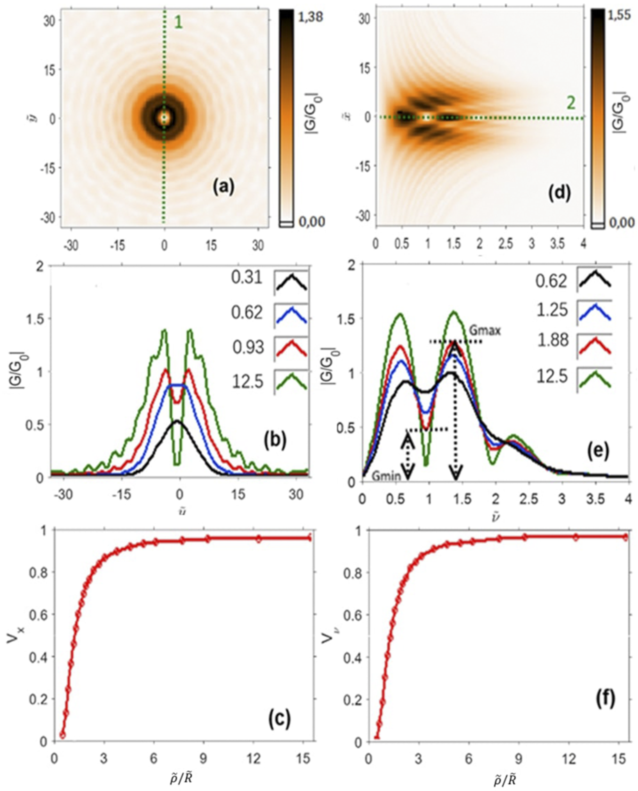

FIG. 5. Normalized modulus of the temporal spectrum [(a), (b), (d), and (e)]: spatial $|G(\tilde{x},\tilde{y},\tilde{\nu}_0,\tilde{z} = \tilde{z}_p)/G_0|$ (a) and spatio-spectral $|G(\tilde{x},\tilde{y} = \tilde{y}_0,\tilde{\nu},\tilde{z} = \tilde{z}_p)/G_0|$ (d) distributions; cross-sections through the beam center $|G(\tilde{x},\tilde{y} = \tilde{y}_0,\tilde{\nu} = \tilde{\nu}_0, \tilde{z} = \tilde{z}_p)/G_0|$ (b) and $|G(\tilde{x} = \tilde{x}_0,\tilde{y} = \tilde{y}_0,\tilde{\nu},\tilde{z} = \tilde{z}_p)/G_0|$ (e) according to lines 1 and 2, respectively; lines of different colors correspond to different ratios ρ/R; and spatial (c) and spectral (f) visibility graphs V_x and V_ν.

Note that these results could be interpreted from a general point of view: each frequency $\widetilde{\nu}$ corresponds to its own characteristic distance $\widetilde{z}_p$. On the other hand, for radiation at the frequency $2\widetilde{\nu}_f(N = 2)$, the aperture is already visible as four Fresnel zones. Figure 5(e) clearly illustrates that there is a spectral minimum for the frequency $2\widetilde{\nu}_f(N = 2) = \widetilde{\nu}_f(N = 4) = 2$ at a given distance on the beam axis. A deep and near-zero spectral notch shows the high efficiency of the proposed filter. Due to its diffraction nature, the depth of the frequency notches becomes smaller as the strengths of apodization increases.

Furthermore, the spectrum amplitude at the beam center $G(\widetilde{x}, \widetilde{y} = \widetilde{y}_0, \widetilde{\nu}, \widetilde{z} = \widetilde{z}_p)$ as a function of $\widetilde{\rho}/\widetilde{R}$ is specified. The spectral distribution is changing with Gaussian width: as $\widetilde{\rho}/\widetilde{R}$ decreases, the profile of the Gaussian beam gets narrower, and at the same time, the spectral gap becomes flatter. The dependency of the normalized modulus of the temporal spectrum in the beam center for several Gaussian parameters $\widetilde{\rho}/\widetilde{R}$ is shown in Figs. 5(b) and 5(e). It is worth noting that when the beam is smaller than the aperture size ($\widetilde{\rho}/\widetilde{R} < 1$), the spectral gap could not be achieved [$\widetilde{\rho}/\widetilde{R} = 0.31$ in Fig. 5(b)].

To evaluate the filtering performance and estimate how deep a frequency gap can be formed both in space and spectrum, we introduce the spatial visibility $V_x = V(\widetilde{x}, \widetilde{y} = y_0, \widetilde{\nu} = \widetilde{\nu}_f, \widetilde{z} = \widetilde{z}_p)$ and spectral visibility $V_\nu = V(\widetilde{x} = \widetilde{x}_0, \widetilde{y} = \widetilde{y}_0, \widetilde{\nu}, \widetilde{z} = \widetilde{z}_p)$,

$$V = \frac{|G_{\max}| - |G_{\min}|}{|G_{\max}| + |G_{\min}|}, \tag{6}$$

where $G_{\max}$ and $G_{\min}$ are the local neighboring maximum and minimum of the spectral amplitude, as shown in Figs. 5(b) and 5(e). The dynamics of these two visibilities are similar and tends to unity as long as the wave front field intensity of the incident THz beam becomes uniform enough, i.e., $\widetilde{\rho}/\widetilde{R}$ tends to unity, as shown in Figs. 5(c) and 5(f).

It can be seen that the visibility grows almost linearly before $\widetilde{\rho}/\widetilde{R}$ increases to 1.5, after which the visibility grows slowly and starts to saturate. A visibility of 70% is obtained at $\widetilde{\rho}/\widetilde{R} = 1.7$, which is sufficient for the operation with a spectral filter.

Special attention should be paid to the fact that in the definition of visibility, the spectral density rather than its squared value was used, which we thought would be more convenient in the THz range. In our opinion, it is more convenient for the THz spectral range. This is due to the fact that in the spectroscopy of the pulsed THz radiation, the wave field is directly measured, and its spectrum is calculated. This is different from the measurement of the pulse intensity (square of a field) usually taking place in the interference technique of the visible and IR spectral range.

Figure 6 shows a scheme of the experimental setup, which is in line with the concept of terahertz pulse time-domain holography (THz PTDH). The InAs crystal located in a strong magnetic field pumped by fs laser (FL) generated THz radiation. The electro-optical sampling method was employed with the CdTe crystal. The iris diaphragm with a thickness of 1.2 mm was used as an aperture. A THz 2-D wavefront modulated by the aperture has been recorded by a scanning pinhole located at a distance $z_{p_1} = 34$ mm, which corresponds to the working distance $\widetilde{z}_{p_1} = 56$ of the FF for the frequency $\nu_f(N = 2) = 0.5$ THz. However, the THz pulses in our experimental setup possessed a longer duration than pulses considered in case 1 in Table I and therefore had a narrower spectrum with a strongly decreasing amplitude at frequency $\nu(N = 2) = 0.5$, which prevented the demonstration of a pronounced minimum. However, it is possible to select any other frequency from the temporal spectrum and using Eq. (3) to determine another distance corresponding to an odd number of Fresnel zones for a point on the optical axis.

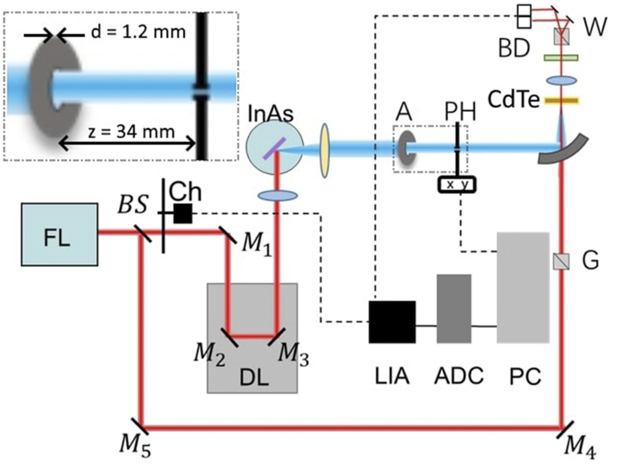

FIG. 6. Experimental setup. FL is the femtosecond laser system, BS is the beam splitter, C is the mechanical chopper, M_1–M_5 are the mirrors, DL is the delay line, A is the circle aperture, InAs is the THz generator, XY is the 2-D raster scanning stage, PH is the scanning pinhole, G is the Glan prism, HWP is the half-wave plate, F is the filter, QWP is the quarter wave plate, W is the Wollaston prism, BD is the balanced detectors, LIA is the lock-in-amplifier, ADC is the digitizer, and PC is the personal computer.

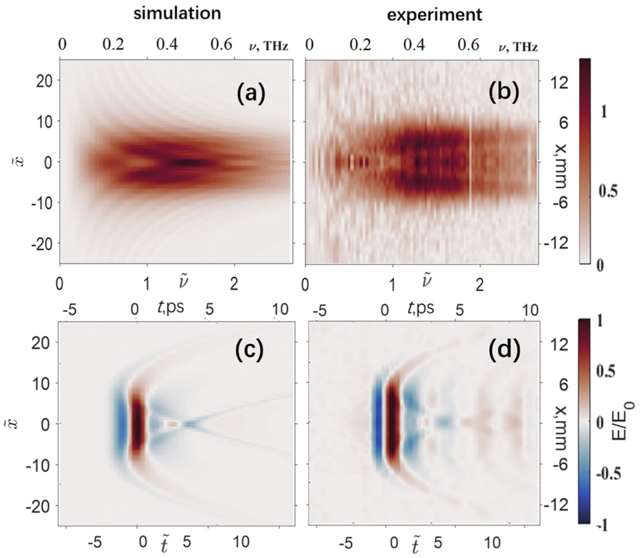

FIG. 7. Results of experimental validation of the proposed FF: spatio-spectral [(a) and (b)] and spatio-temporal [(c) and (d)] distributions of the transverse component for the computer-synthesized [(a) and (c)] and experimentally measured [(b) and (d)] data at distance $\widetilde{z}_{p_2} = 22$.

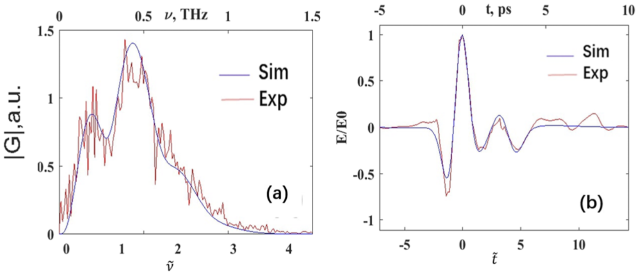

FIG. 8. Results of experimental validation of the proposed FF: spatio-spectral (a) and spatio-temporal (b) distributions of the transverse component for the computer-synthesized (blue line) and experimentally measured (red line) data corresponding to the axial cross-sections of Fig. 7 at distance $\widetilde{z}_{p_2} = 22$.

Thus, we defined parameters of case 2 in Table I: THz pulse duration $\tau = 0.7$ ps with the corresponding spectrum interval approximately from 0.1 THz to 1.5 THz. Thus, the central frequency ν_0 which corresponds to the maximum of the spectral amplitude was equal to 0.33 THz. For the aperture radius $\widetilde{R} = 6.4$ used in our calculations, the corresponding characteristic distance is $\widetilde{z}_{p_2} = 22$ [$z_{p_2} = 20$ mm as shown on Fig. 2(a)]. For these parameters, the corresponding spatio-spectral [Figs. 7(a) and 7(b)] and spatio-temporal [Figs. 7(c) and 7(d)] distributions were calculated from computer-synthesized and experimentally measured data. The cross-section view of both spatio-spectral and spatio-temporal distributions has been compared in Fig. 8. Note that experimental temporal and spectral data were processed by block-matching 3D protocol (BM3D) adapted for pulsed THz fields in Ref. 19.

III. CONCLUSION

In summary, a tunable Fresnel notch filter for N-fold frequencies of a broadband single-cycle THz wavefront has been proposed, investigated, and experimentally verified. According to the proposed design, these frequencies arrive at the axial position from an even number of Fresnel zones and may be adjusted by varying the observation distance and the aperture radius. The size of the filtering aperture in our calculations and experiments was chosen from several to several ten times larger than the central wavelength of radiation. Due to the wide spectrum of the THz pulse, diffraction was generally non-paraxial. The condition for both spatially-homogeneous and Gaussian waves has been considered as the initial conditions. For case 1, when $\widetilde{R} = 10.7$ and $\widetilde{\rho}/\widetilde{R} = 1.7$, it has been demonstrated that the visibility V of the spectral notch of the single-cycle THz pulse after passing the aperture is 70%, which is sufficient for practical operation. It was also shown that the portion of evanescent waves is about 7% in a Gaussian beam passing through the aperture. However, with rather a small number of evanescent waves, the ratio of the longitudinal and transverse components can be significant and in some regions reach 35%.

A possible practical implementation of the proposed filter may be a rigidly coupled configuration of two diaphragms: the first initializes the spectral modulation phenomenon carefully studied in the given work, whereas the second one, located exactly at a distance $\widetilde{z}_p$, blocks the THz field on the periphery, where the desired modulation is absent. The measured results agree well with the simulation and theory. We believe that the proposed filter may contribute to the tasks of the generation of structured longitudinal THz fields and relevant applications. Strong diffraction effects are important to be taken into account in pulse THz spectroscopy. Thus, the presence of an aperture on the measured sample can give a dip in the spectrum of the transmitted radiation of a diffraction nature when measuring the sample transmission, which can be interpreted as the absorption line of the material.

ACKNOWLEDGMENTS

This work was supported by the Russian Foundation for Basic Research (Grant No. 18-32-20215\18).

DATA AVAILABILITY

The data that support the findings of this study are available from the corresponding author upon reasonable request.

REFERENCES

[1] H.-T. Chen, J. F. O'Hara, A. K. Azad, and A. J. Taylor, "Manipulation of terahertz radiation using metamaterials," Laser Photonics Rev. **5**, 513–533 (2011).

[2] J. Lee, M. Seo, D. Park, D. Kim, S. Jeoung, C. Lienau, Q.-H. Park, and P. Planken, "Shape resonance omni-directional terahertz filters with near-unity transmittance," Opt. Express **14**, 1253 (2006).

[3] R. Mendis, A. Nag, F. Chen, and D. M. Mittleman, "A tunable universal terahertz filter using artificial dielectrics based on parallel-plate waveguides," Appl. Phys. Lett. **97**, 131106 (2010).

[4] S. F. Busch, S. Schumann, C. Jansen, M. Scheller, M. Koch, and B. M. Fischer, "Optically gated tunable terahertz filters," Appl. Phys. Lett. **100**, 261109 (2012).

[5] A. Siemion, "Terahertz diffractive optics—Smart control over radiation," J. Infrared, Millimeter, Terahertz Waves **40**, 477–499 (2019).

[6] J. C. Wiltse, "Zone plate designs for terahertz frequencies," Proc. SPIE **5790**, 167–179 (2005).

[7] S. Wang, T. Yuan, E. D. Walsby, R. J. Blaikie, S. M. Durbin, D. R. S. Cumming, J. Xu, and X.-C. Zhang, "Characterization of T-ray binary lenses," Opt. Lett. **27**, 1183–1185 (2002).

[8] E. D. Walsby, S. Wang, J. Xu, T. Yuan, R. Blaikie, S. M. Durbin, X.-C. Zhang, and D. R. S. Cumming, "Multilevel silicon diffractive optics for terahertz waves," J. Vac. Sci. Technol., B **20**, 2780–2783 (2002).

[9] P. M. Solyankin, M. N. Esaulkov, I. A. Chernykh, I. V. Kulikov, M. L. Zanaveskin, A. R. Kaul, A. M. Makarevich, D. I. Sharovarov, O. E. Kameshkov, B. A. Knyazev *et al.*, "Terahertz switching focuser based on thin film vanadium dioxide zone plate," J. Infrared, Millimeter, Terahertz Waves **39**, 1203–1210 (2018).

[10] M. Born and E. Wolf, *Principles of Optics: Electromagnetic Theory of Propagation, Interference and Diffraction of Light* (Elsevier, 2013).

[11] R. Martínez-Herrero, P. M. Mejías, and G. Piquero, *Characterization of Partially Polarized Light Fields* (Springer Science & Business Media, 2009), Vol. 147.

[12] Z. Wu, X. Wang, W. Sun, S. Feng, P. Han, J. Ye, Y. Yu, and Y. Zhang, "Vectorial diffraction properties of THz vortex Bessel beams," Opt. Express **26**, 1506–1520 (2018).

[13] S. Freer, A. Gorodetsky, and M. Navarro-Cia, "Beam profiling of a commercial lens-assisted terahertz time domain spectrometer," IEEE Trans. Terahertz Sci. Technol. (published online).

[14] A. Koulouklidis, V. Y. Fedorov, and S. Tzortzakis, "Spectral bandwidth scaling laws and reconstruction of THz wave packets generated from two-color laser plasma filaments," Phys. Rev. A **93**, 033844 (2016).

[15] K.-L. Yeh, J. Hebling, M. C. Hoffmann, and K. A. Nelson, "Generation of high average power 1 kHz shaped THz pulses via optical rectification," Opt. Commun. **281**, 3567–3570 (2008).

[16] V. G. Bespalov, A. A. Gorodetskiĭ, I. Yu. Denisyuk, S. A. Kozlov, V. N. Krylov, G. V. Lukomskiĭ, N. V. Petrov, and S. É. Putilin, "Methods of generating

superbroadband terahertz pulses with femtosecond lasers," J. Opt. Technol. **75**, 636–642 (2008).

[17] A. A. Andreev, V. G. Bespalov, A. A. Gorodetskii, S. A. Kozlov, V. N. Krylov, G. V. Lukomskii, E. V. Novoselov, N. V. Petrov, S. E. Putilin, and S. A. Stumpf, "Generation of ultrabroadband terahertz radiation under optical breakdown of air by two femtosecond pulses of different frequencies," Opt. Spectrosc. **107**, 538–544 (2009).

[18] N. V. Petrov, M. S. Kulya, A. N. Tsypkin, V. G. Bespalov, and A. Gorodetsky, "Application of terahertz pulse time-domain holography for phase imaging," IEEE Trans. Terahertz Sci. Technol. **6**, 464–472 (2016).

[19] M. Kulya, N. V. Petrov, A. Tsypkin, K. Egiazarian, and V. Katkovnik, "Hyperspectral data denoising for terahertz pulse time-domain holography," Opt. Express **27**, 18456 (2019).

[20] A. A. Ezerskaya, D. V. Ivanov, S. A. Kozlov, and Y. S. Kivshar, "Spectral approach in the analysis of pulsed terahertz radiation," J. Infrared, Millimeter, Terahertz Waves **33**, 926–942 (2012).

[21] M. S. Kulya, V. A. Semenova, V. G. Bespalov, and N. V. Petrov, "On terahertz pulsed broadband Gauss-Bessel beam free-space propagation," Sci. Rep. **8**, 1390 (2018).

[22] M. Kulya, V. Semenova, A. Gorodetsky, V. G. Bespalov, and N. V. Petrov, "Spatio-temporal and spatiospectral metrology of terahertz broadband uniformly topologically charged vortex beams," Appl. Opt. **58**, A90 (2019).

[23] M. S. Kulya, N. S. Balbekin, A. A. Gorodetsky, S. A. Kozlov, and N. V. Petrov, "Vectorial terahertz pulse time-domain holography for broadband optical wavefront sensing," Proc. SPIE **11279**, 112790D (2020).